Sensitive Damage Detection of Reinforced Concrete Bridge Slab by "Time-Variant Deconvolution" of SHF-Band Radar Signal

Takahiro Yamaguchi, Tsukasa Mizutani, *Member, IEEE*, Minoru Tarumi, and Di Su

***Abstract*— In this paper, we focus on ground-penetrating radar (GPR) for infrastructural health monitoring, especially for the monitoring of reinforced concrete (RC) bridge slab. Due to the demand of noncontact and high-speed monitoring technique which can handle vast amounts of aging infrastructures, GPR is a promising tool. However, because radar images consist of many reflected waves, they are usually difficult to interpret. Furthermore, the spatial resolution of system is not enough considering the thickness of target damages, cracks, and segregation are millimeter-to-centimeter order while the wavelength of ordinary GPR ultrahigh-frequency band is over 10 cm. To address these problems, for the purpose of sensitive damage detection, we propose a new algorithm based on deconvolution utilizing a super high-frequency (SHF) band system. First, a distribution of reflection coefficient is inversely estimated by 1-D bridge slab model. Because concrete is found to be a lossy medium at SHF band, we consider the attenuation of signal in deconvolution. The algorithm is called "time-variant deconvolution" in this paper. After the validation by simulation, the effects of the algorithm and frequency band on damage detection accuracy are evaluated by a field experiment. Though the results show a 1-mm horizontal crack is not detected by measured waves, when it is filled with water, it is detected by time-variant deconvolution. Moreover, the 1-mm dried crack is detected only by time-variant deconvolution at SHF band, which greatly emphasizes the peaks of the reflection coefficient of the crack.**

***Index Terms*— Ground-penetrating radar (GPR), infrastructural health monitoring, thin cracks and segregation detection, time-variant deconvolution.**

I. Introduction

THE ground-penetrating radar (GPR) is a promising tool for nondestructive and rapid infrastructure health monitoring. In particular, road pavement and bridge slab assessment are appropriate examples of GPR method [1]–[13]. In terms of road pavement assessment, thickness and deterioration evaluation of existing asphalt pavement and quality control of constructed asphalt pavement are the main topics of GPR method. For example, Al-Qadi and Lahouar [6] and Zhao and Al-Qadi [9] introduce common midpoint method to successfully estimate asphalt pavement thickness. Benedetto *et al.* [7] summarized the signal processing techniques used to produce radar images for road inspections. In terms of bridge slab assessment, Alani *et al.* [2] provided a case study, in which the deteriorated area of bridge slab is evaluated by the horizontal cut of 3-D radar images.

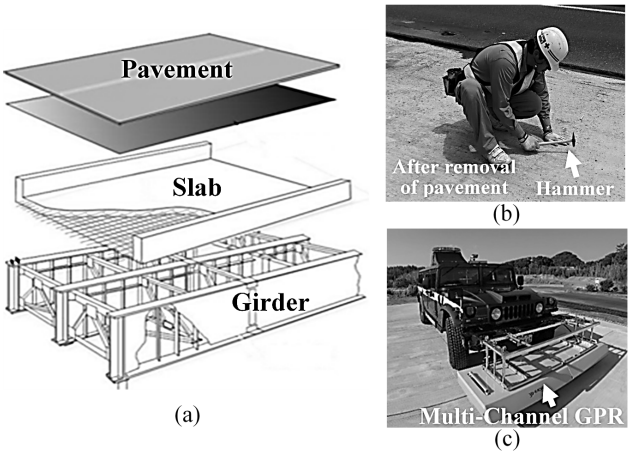

Fig. 1. Damage detection of RC bridge slab. (a) Schematic view of RC bridge slab, taken from [15]. (b) Hammer sounding test. (c) Ordinary GPR system.

As an example of developed countries, in Japan, 40% of 700 000 bridges in service are going to be over 50 years old in 10 years and 60% of the whole 2 trillion-yen (U.S. $20 billion) highway-structure maintenance cost is accounted for bridge slab repairment and replacement [14]. On the other hand, ordinary inspection method such as hammer sounding test needs a traffic control, removal of pavement, and careful inspection of all the corresponding areas by skilled inspectors [Fig. 1(a) and (b)] [15]. GPR mounted on inspection car has the possibility and is the limited equipment to detect damages inside bridge slab below asphalt pavement without a removal of pavement noncontact and high speed, up to 80 km/h, enabling us to monitor a vast number of infrastructure stocks utilizing a limited amount of maintenance resource [Fig. 1(c)].

Manuscript received February 7, 2018; revised May 17, 2018 and July 23, 2018; accepted August 16, 2018. Date of publication September 19, 2018; date of current version February 25, 2019. This work was supported in part by Cross-ministerial Strategic Innovation Promotion Program, "Infrastructure Maintenance, Renovation and Management (Program Director: Prof. Y. Fujino from the Institute of Advanced Sciences, Yokohama National University)," and in part by the Government of Japan and Japan Science and Technology Agency. *(Corresponding author: Takahiro Yamaguchi.)*

T. Yamaguchi and D. Su are with the Department of Civil Engineering, Graduate School of Engineering, The University of Tokyo, Tokyo 113-8656, Japan (e-mail: tyamaguchi@bridge.t.u-tokyo.ac.jp; su@bridge.t.u-tokyo.ac.jp).

T. Mizutani is with the Institute of Industrial Science, The University of Tokyo, Tokyo 153-8505, Japan (e-mail: mizu-t@iis.u-tokyo.ac.jp).

M. Tarumi is with the C. E. Management Integrated Laboratory Co., Ltd., Osaka 599-8237, Japan (e-mail: m-tarumi@dksiken.co.jp).

Digital Object Identifier 10.1109/TGRS.2018.2866991

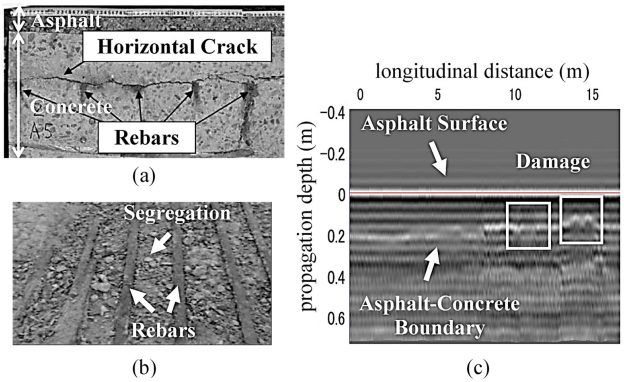

Fig. 2. Target deficiencies and image of GPR method. (a) Horizontal crack. (b) Segregation. (c) Typical radar image of bridge slab.

Target deficiencies are millimeter-order thickness horizontal cracks and segregations inside reinforced concrete (RC) bridge slab, which often occur above rebars [Fig. 2(a) and (b)]. A horizontal crack and segregation are considered to be a millimeter-order thin air layer and centimeter-order sand-like concrete layer, respectively. The latter is occurred when horizontal cracks are progressed. In terms of maintenance management, the existence of water inside damage is also important because it is known to accelerate the deterioration of concrete. Road administrators may need to detect thin cracks before they progress to severe damages such as holes because they may cause serious accidents.

In GPR method, an inspector detects anomalies from a large amount of cross-sectional radar image data measured by each sensor of a multichannel GPR system [Fig. 1(c)]. The problem is radar images are usually difficult to interpret, as shown in Fig. 2(c). Another problem is that because GPR is generally considered as a monitoring tool for the whole condition of concrete layer and reinforcement rebar inside RC slab, the spatial resolution of typical GPR system is not enough to detect millimeter-order thickness thin cracks in spite of its practical necessity. Because a typical bridge slab radar image consists of many reflected waves from each layer and embedded materials, Mizutani *et al.* [16] proposed an algorithm to automatically detect damages by a cross correlation of healthy and damaged section signals. However, the algorithm could not detect smaller than 10-mm horizontal cracks under dry condition from the measurement data of real bridge slab model. The target of the research is to develop a system which has the sensitivity to detect millimeter-order small cracks to help road administrators' decisions.

In this paper, we propose a new damage detection algorithm based on deconvolution. Utilizing transmitted and received electromagnetic waves, "reflection coefficient distribution" is inversely estimated. The research consists of two objectives. First, to develop a more sensitive GPR system, in addition to typical GPR frequency band, very high-frequency (VHF) and ultrahigh-frequency (UHF) band (30 MHz–3 GHz), higher frequency band, and super high-frequency (SHF) band (3–20 GHz) are adopted. Second, the inverse problem is solved by ordinary "time-invariant deconvolution" and "time-variant deconvolution," where the attenuation effect in high-frequency range is considered. The proposed algorithms are applied to simulated waves and measurement data of a constructed real bridge slab model to evaluate the effect of the algorithms and frequency bands on damage detection accuracy.

The rest of this paper is followed by five sections. Section II defines the inverse problem. Time-invariant and time-variant deconvolution are also introduced in this section. Section III discusses the reflection coefficient and attenuation coefficient of concrete medium as a basis for the following discussion. Sections IV and V present the details of the simulation and field experiment. Estimation results are displayed to show the accuracy of each deconvolution algorithm. Section VI summarizes this paper.

II. Inverse Analysis of Bridge Slab Model

A. Problem Definition

In most cases, even a pulse radar with wide frequency range, received signals are distorted to lower the resolution of images. "Deconvolution" is an operation which is designed to recover a transmitted signal waveform from a received signal utilizing retained transmitted signal information. The deconvolution is categorized in terms of an operation domain: 1) time domain or 2) frequency domain, and the waveform of the transmitted signal, a) known or b) unknown.

If the waveform of the transmitted signal is known, 1)-a) or (2)-a), the deconvolution problem falls into a classical signal processing problem as discussed in [10], [17], and [18]. For example, Zhao and Al-Qadi [10] successfully estimated the thickness of thin asphalt layer by deconvolution. To avoid the ill-posed nature of the inverse filter of transmitted signal, the deconvolution problem is solved by the optimization of regularization problem. If the waveform of the transmitted signal is not known, 1)-b) or 1)-(b), signal processing techniques, such as predictive theory and blind deconvolution (ICA), are applied in either domain utilizing the stochastic characteristics of the signals [19], [20].

In the case of GPR method, the waveform of the transmitted signal is known. When the transmitted wave is attenuated inside medium, however, ordinary deterministic deconvolution cannot be applied. Though some research focus on the compensation of the attenuation effect of transmitted signal at each depth [21], [22], when the transmitted wave reflected at each layer boundary is superposed in short time range, estimation accuracy decreases, as is the case with bridge slab GPR images.

Assuming the transmitted signal is exactly known at each depth, the reflection coefficient at each medium boundary is inversely estimated from the transmitted and received signal by deconvolution. In this paper, bridge slab is represented by 1-D multilayered medium model as illustrated in Fig. 3. From Fig. 3, when a reflection coefficient distribution is accurately estimated, the existences of damages are clearly represented by the peaks of the medium boundaries between the damages and surrounding concrete medium. The target of the research is to propose an algorithm to accurately estimate a reflection coefficient distribution considering the attenuation effect of concrete medium.

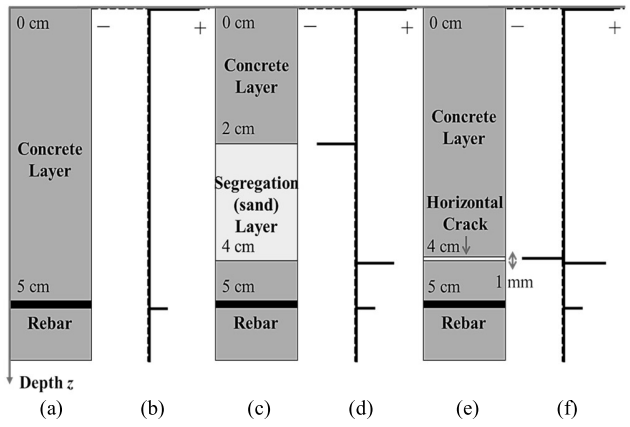

Fig. 3. 1-D multilayered medium model of bridge slab. (a) Healthy section (b) Reflection coefficient of healthy section. (c) Segregation (d) Reflection coefficient of segregation. (e) Horizontal crack. (f) Reflection coefficient of horizontal crack.

In 1-D bridge slab model, the received signal is the convolution (the symbol $*$) of the transmitted signal and reflection coefficient distribution

$$E_{\text{obs}}(t) = \Gamma(z) * E_o(t) \tag{1}$$

where E_{obs}, E_o, and Γ denotes the received signal, transmitted signal, and reflection coefficient and z is the depth related with the propagation time t by $z = ct/2$, where c is the propagation velocity. The inverse problem is to estimate Γ from known E_{obs} and E_o. As for measurement data, because t is discrete and finite, all the variables in (1) are discrete and finite.

B. "Time-Invariant Deconvolution"

In the frequency domain, from the Fourier transform of both sides of (1), convolution turns into product at each frequency by Wiener–Khinchin theorem. Γ is estimated by

$$\Gamma(f) = E_{\text{obs}}(f)/E_o(f) \tag{2}$$

using E_{obs} and E_o at each frequency f. Indicated by Zhao and Al-Qadi [10], however, because of the losses of certain frequency components in measurement data of E_o, "division-by-zero" problem occurs, which necessitates the algorithm to obtain the approximate solution of Γ.

In the time domain, because all the variables are discrete and finite, (1) is represented by the matrix equation

$$\widehat{\boldsymbol{E}}_{\boldsymbol{obs}} = \boldsymbol{E_o} \times \widehat{\Gamma} \tag{3}$$

where $\widehat{\boldsymbol{E}}_{\boldsymbol{obs}}$ is the received signal vector and $\widehat{\boldsymbol{\Gamma}}$ is the reflection coefficient vector. $\boldsymbol{E_o}$ is the transmitted signal matrix consisted of time-shifted E_o

$$\boldsymbol{E_o} = \begin{pmatrix} E_o(0) & E_o(T) & \cdots & E_o(\Delta t) \\ E_o(\Delta t) & E_o(0) & \cdots & E_o(\Delta t) \\ \vdots & \vdots & \ddots & \vdots \\ E_o(T) & E_o(T-\Delta t) & \cdots & E_o(0) \end{pmatrix} \tag{4}$$

when t is confined from 0 to T discretized with time step Δt. T is corresponding to the measurement time length, and Δt is the reciprocal of the maximum frequency of the system.

If $\boldsymbol{E_o}$ has an inverse matrix, $\widehat{\boldsymbol{\Gamma}}$ is estimated from $\widehat{\boldsymbol{E}}_{\boldsymbol{obs}}$ by

$$\widehat{\boldsymbol{\Gamma}} = \boldsymbol{E_o^{-1}} \times \widehat{\boldsymbol{E}}_{\boldsymbol{obs}} \tag{5}$$

where $\boldsymbol{E_o^{-1}}$ is the inverse matrix of $\boldsymbol{E_o}$. If all the frequencies are properly transmitted and received, simultaneous equation (5) has a reasonable solution. The problem is, again, that because of the losses of frequency components in E_o, $\widehat{\boldsymbol{\Gamma}}$ estimated by (5) shows an unreasonable value because of "division-by-zero" problem, as indicated in the frequency domain [10]. To overcome this problem, the pseudoinverse matrix $\boldsymbol{E_o^+}$ is estimated by singular value decomposition [23]. $\widehat{\boldsymbol{\Gamma}}$ is estimated by

$$\widehat{\boldsymbol{\Gamma}} \approx \boldsymbol{E_o^+} \times \widehat{\boldsymbol{E}}_{\boldsymbol{obs}} \tag{6}$$

replacing $\boldsymbol{E_o^{-1}}$ by $\boldsymbol{E_o^+}$. $\widehat{\boldsymbol{\Gamma}}$ estimated by (6) is the least-squares approximation solution of (3). The threshold of the singular value to construct $\boldsymbol{E_o^+}$ is obtained from the actual data and set constant in this paper for the comparison of the algorithms.

C. Time-Variant Deconvolution

Actually, because of the attenuation effect, the transmitted signal E_o is time dependent. In time-variant deconvolution, because of the time dependence of E_o, the Fourier transform of (1) is not simple. In the time domain, (1) is rewritten as

$$E_{\text{obs}}(t) = \Gamma(z) * E_t(t) \tag{7}$$

using the time-variant transmitted signal E_t

$$E_t(t) = F_a(E_o(t), t) \tag{8}$$

where F_a is a filter representing the attenuation effect, which is a function of t.

Follow the same procedure for deriving (3), (7) is represented by the matrix equation

$$\widehat{\boldsymbol{E}}_{\boldsymbol{obs}} = \boldsymbol{E_t} \times \widehat{\Gamma} \tag{9}$$

where $\boldsymbol{E_t}$ is the transmitted signal matrix considering the attenuation effect. $\boldsymbol{E_t}$ consists of the time-shifted and attenuated transmitted signal E_t at each time

$$\boldsymbol{E_t} = \begin{pmatrix} E_0(0) & E_1(T) & \cdots & E_0(\Delta t) \\ E_0(\Delta t) & E_1(0) & \cdots & E_N(2\Delta t) \\ \vdots & \vdots & \ddots & \vdots \\ E_1(T) & E_1(T-\Delta t) & \cdots & E_N e(0) \end{pmatrix} \tag{10}$$

where E_n is the transmitted signal at $t = n\Delta t$. $\widehat{\boldsymbol{\Gamma}}$ is approximately estimated by the pseudoinverse matrix $\boldsymbol{E_t^+}$ by the same procedure for deriving (6).

In this paper, the multireflection of the transmitted signal E_t is not considered because the attenuation effect is considered to be large in the multireflection wave, whose effect is discussed in Section III. Furthermore, in the multireflection process, the wave gradually loses its energy depending on the value of each boundary reflection coefficient. The transmission coefficient of each medium boundary should be considered to estimate the exact transmitted signal E_t. However, because the existence and depth of each boundary is not known *a priori* and the target damages are assumed to

be just below the concrete surface, the transmission loss was ignored except for the transmission loss of concrete surface. Actually, the reflection coefficient of the bottom boundary of damage is underestimated. Nevertheless, from the obtained permittivity and transmission loss (18) explained in Section III, the expected error is smaller than 10%, which is not substantial for damage detection as discussed in Section V. The effect of asphalt and other types of pavement is not thoughtfully investigated in this research. By utilizing the electromagnetic properties of pavement, the same algorithm is expected to be applicable setting an appropriate frequency range and power of the transmitted signal. The3-D effect and inhomogeneity of the propagating media are out of scope in this paper [24], [25].

D. Reduction of Noise Effect

In actual measurement, (7) is disturbed with observation noise, making the inverse problem ill conditioned

$$E_{\mathrm{obs}}(t) = \Gamma(z) * E_t(t) + n(t) \tag{11}$$

where $n(t)$ is the noise term. Because of the attenuation effect, E_t becomes smaller at deeper depth. Therefore, the effect of n becomes relatively large, causing the unstable behavior of estimated Γ at deeper depth. Because the attenuation coefficient of concrete medium is frequency-dependent as will be shown in Section III, especially the noise of higher frequency component is dominant. A signal processing is needed which prevents the inverse solution from diverging when the power of the reflected signal is close to or falls below that of n.

In this paper, to avoid the unstable behavior of the inverse problem, Wiener filter is adopted. The detailed derivations are explained in Appendix A. The Wiener filter H_w is a frequency domain time-invariant filter to obtain a noise-free signal $\Gamma \times E_t$ from a noise-contaminated signal E_{obs} in (11)

$$H_w(f) = \frac{P_{\Gamma \times E_t}(f)}{P_{\Gamma \times E_t}(f) + P_n(f)} \tag{12}$$

where H_w is the function of the power spectrum P of each signal [26]. By applying H_w at each t using Γ at $z = ct$ and E_t at t, also explained in Appendix A, the revised transmitted signal E_t' is defined as

$$E_t'(f) = \frac{E_t(f)}{H_w(f)} \tag{13}$$

and $\widehat{\mathbf{\Gamma}}$ can be estimated by the same procedure for deriving (6) using the pseudoinverse matrix of revised $\boldsymbol{E_t^\circ}$.

The problem is H_w at each t in (12) cannot be determined because Γ is unknown. Nevertheless, the estimation results indicate that if an appropriate initial Γ_0 is assumed, Γ is properly estimated using the exactly known E_t as will be shown in Section IV. In Section IV, the sensitivity of assumed signal-to-noise ratio (SNR) is also discussed. The electromagnetic properties of concrete to estimate E_t are discussed in Section III.

III. Electromagnetic Characteristics of Concrete Medium at SHF Band

The electromagnetic properties of concrete are investigated for the purpose of structural health monitoring [27]–[31].

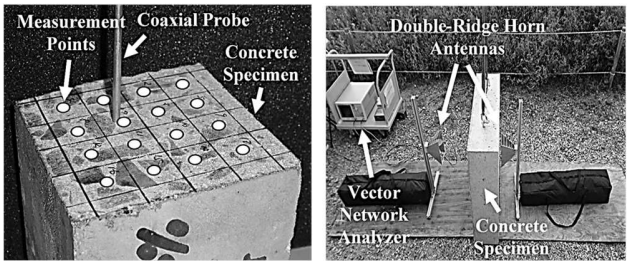

Fig. 4. Measurements of electromagnetic properties of concrete at SHF band. (a) Coaxial probe method. Measurement points are the centers of the squares of the lattice shape marked on the specimen surface. (b) Free-space method.

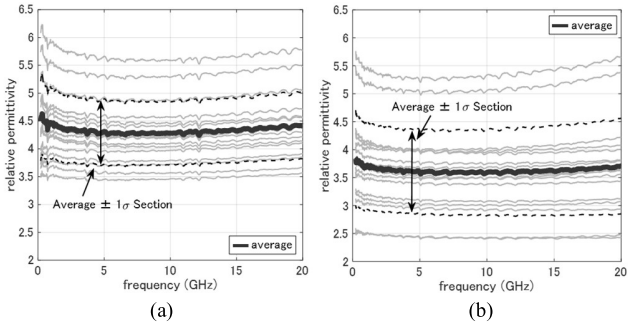

Fig. 5. Relative permittivity of concrete specimen. (a) W/C = 30%. (b) W/C = 65%. Thin lines represent each measurement point shown in Fig. 4(a). Bold line shows the average. Average $\pm 1\sigma$ (σ: standard deviation) section is also shown by dashed lines.

However, there is little research about the electromagnetic properties at SHF band because the frequency range of an ordinary GPR system is limited to VHF and UHF bands in terms of bridge slab concrete especially constructed by the Japanese standard configuration. Therefore, two types of measurements were conducted; the permittivity was measured by coaxial probe method; the attenuation coefficient was measured by free-space method as shown in Fig. 4 [32], [33]. The obtained permittivity and attenuation characteristics are consistent with the parameters in the case of concrete structure of buildings in other countries [30], [31]. For example, the obtained permittivity and conductivity at 3-GHz converted from the obtained attenuation coefficient are within the range of the parameters estimated by Patriarca *et al.* [30], and the conductivity shows the same frequency dependence. In this paper, the permeability of concrete is assumed to be the same as the permeability of vacuum μ_0.

A. Relative Permittivity

In coaxial probe method, the relative permittivity of a contacted specimen surface is measured by coaxial probe as shown in Fig. 4(a). The developed system, whose probe diameter is designed to measure at SHF band, was validated with a standard methanol specimen referring to the theoretical electromagnetic properties of methanol.

Fig. 5 displays the relative permittivity of the concrete specimen from 100 MHz to 20 GHz when water–cement ratio (W/C) is 30% and 65%, which are the lower and upper bounds of Japanese normal concrete slab standard; actual

concrete slab is ranging between 30% and 65%. Each thin line in Fig. 5 shows the relative permittivity at each measurement point of the surface marked in a lattice shape as shown in Fig. 4(a). Because concrete is a heterogeneous material, the measured permittivity was affected by local aggregate, cement and air. However, because the electromagnetic characteristics of the whole projection area of the antennas affect the results, when the number of the measurement points is sufficiently large, the average value of the permittivity measured at each section of the specimen surface is considered to appropriately represent the relative permittivity of concrete.

The bold lines, which is corresponding to the averages, and the dashed lines, which is corresponding to the $\pm 1\sigma$ (σ: standard deviation) section of the averages in Fig. 5, indicate the relative permittivity of concrete ε_c is about

$$\varepsilon_c \cong 4 = \text{constant} \tag{14}$$

widely ranging from 100 MHz to 20 GHz, consistent with [27]–[31]. For example, the 10% variation of the relative permittivity in Fig. 5 affects the depth estimation, corresponding to the 10% scale change of reflection coefficient distribution, which is not considered to have large effects on damage detection accuracy in this research. The theoretical value of reflection coefficient in Section V is also obtained using (14). Nevertheless, the effect of the variation of the relative permittivity is not substantial comparing to the detected peak values of the damages, as discussed in Section V.

In this paper, from (14), the relative permittivity of concrete is assumed to be 4 at SHF band. Air is 1, water is 80, sand is 2, and sand with water is 10. Because sand is almost air, the relative permittivity ε_s is determined to correspond with [12] and [13] at UHF band. Actually, the imaginary part of ε_c relating to the attenuation coefficient is also measured by coaxial probe method. However, the repeatability was low and the results sometimes showed negative values. Therefore, free-space method was conducted to obtain the electromagnetic properties of the wider area of the concrete specimen.

B. Attenuation Coefficient

In free-space method, by placing a specimen between transmitting and receiving antennas set opposite sides, the attenuation coefficient is estimated from the received wave intensity. A field experiment was conducted utilizing the measurement system consisted of double-ridge horn antennas and a vector network analyzer as shown in Fig. 4(b). The thickness of the measured concrete specimens was 3, 5, 10, 15, 20, 25, and 30 cm. The specimens are the common-type concrete following the Japanese standard of RC bridge slab, applicable to the most of RC slabs in service in Japan.

In free-space method, the received electric field intensity E_r is represented by the transmitted electric field intensity E_t, transmission loss at the specimen surface T, attenuation loss inside the specimen L, free-space loss F, and measurement system loss G

$$E_r(f) = T(f)L(f)F(r, f)G(f)E_t(f) \tag{15}$$

where r is a distance between the two antennas. Without the specimen, the received electric field intensity E'_r is rewritten as

$$E'_r(f) = F(r, f)G(f)E_t(f) \tag{16}$$

assuming the same measurement configuration. Divide (15) by (16), the signal intensity ratio E_r/E'_r is written as

$$E_r/E'_r = T(f)L(f) \tag{17}$$

which only depends on T and L. T and L are written as

$$T(f) = \frac{4\sqrt{\varepsilon(f)}}{(1+\sqrt{\varepsilon(f)})^2} \tag{18}$$

$$L(f) = e^{-\alpha(f)d} \tag{19}$$

where ε, α, and d denote the relative permittivity, attenuation coefficient, and thickness of the specimen, respectively. T is derived from the multiplication of the transmission coefficient from air to specimen and from specimen to air given by Fresnel equations [34]. Assuming the relative permittivity of concrete is constant, T is independent of frequency f. Substituting (18) and (19) into (17) and taking the logarithm of both sides of (17), it converts to

$$\log(E_r/E'_r) = -\alpha(f)d + \text{constant} \tag{20}$$

where the log signal intensity ratio $\log(E_r/E'_r)$ is proportional to d. By plotting $\log(E_r/E'_r)$ against d, the slope of the line corresponds to the attenuation coefficient at each f.

Fig. 6(a) shows $\log(E_r/E'_r)$ against d at each f. Fig. 6(b) shows estimated α against f. To evaluate the effect of the antenna and specimen size, α was estimated changing r. From Fig. 6(b), the conclusion is the effect of r is small and the repeatability is high. From Fig. 6(b), α is proportional to f

$$\alpha(f) \approx \beta f \tag{21}$$

$$\beta_c \cong 6.8 \times 10^{-9}\ \text{Np} \times \text{s} \times \text{m}^{-1} \tag{22}$$

with high R^2 where β_c is the proportionality constant of concrete at SHF band, which is adopted in simulation and time-variant deconvolution algorithm in this paper.

On the other hand, purely theoretical point of view, α is represented by the $\tan\delta$, permittivity ε, and permeability μ of the material. From (21) and (22), the $\tan\delta$ of concrete $\tan\delta_c$ is considered to be constant

$$\tan\delta_c \cong 0.31 \tag{23}$$

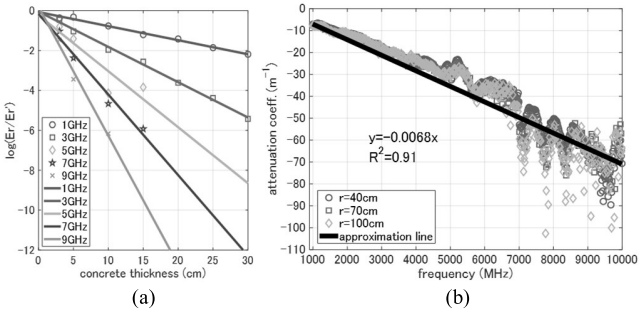

(a) (b)

Fig. 6. Attenuation coefficient of concrete specimens. (a) Log signal intensity ratio against concrete thickness at each frequency. Slopes of lines correspond to attenuation coefficient at each frequency. (b) Dots show attenuation coefficient against frequency when antenna distance $\boldsymbol{r}$ is 40, 70, and 100 cm. Line shows least-squares approximation line of averages of dots.

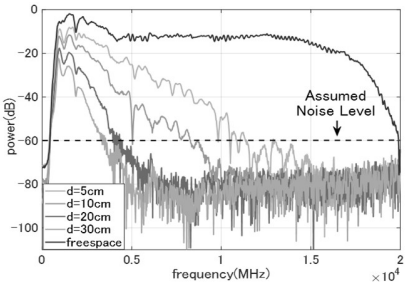

Fig. 7. Power spectra of concrete specimens by free-space method changing concrete thickness d. $d = 5, 10, 20$, and 30 cm are shown here.

at SHF band. Even if tanδ is not constant, the same time-variant deconvolution algorithm is applicable to the measured signals by approximating α and tanδ as the function of f. From (23), the conclusion is concrete is a lossy material at SHF band which necessitates the time-variant deconvolution. Equation (23) is also consistent with the specimens of other research in the case of concrete structure of buildings [30], [31].

IV. Validation of Algorithms by Simulation

To validate the algorithms proposed in Section II, a simulation was conducted. Without noise, because the reflection coefficient is exactly estimated, the damage detection accuracy depends only on the operating frequency range, which determines the resolution of the system. However, because of noise, the accuracy decreases depending on the efficiency of the noise reduction filter. In simulation, the efficiency of the Wiener filter H_w was evaluated.

A. Simulation Configuration and Conditions

In simulation, noise is added to a received signal to validate the effect of the filter H_w. The received signal is synthesized by a 1-D bridge slab model considering the attenuation effect. The received signal itself is an analytical solution of the summation of the reflected waves at layer boundaries, as explained in detail in Appendix B. In the simulation, as stated in Section II, multireflection was neglected. The simulated signals were compared to the field experiment data to confirm the multireflection and 3-D effect was small.

An analyzed case was a 10-mm thickness dried horizontal crack inside concrete medium 4 cm below the concrete surface. The input signal was measured by a field experiment using a steel plate. The power was set 0 dBm, which is reasonable considering the regulations of bridge slab measurement. Assuming a white Gaussian noise, the initial reflection coefficient Γ_0 and the assumed noise level P_n were changed while the added noise level P was -60 dB. The noise level P was obtained from Fig. 7 in the case of free-space method changing concrete thickness as shown in Fig. 4(b), where the noise effect was observed from -60 dB around 5 GHz. To be more precise, P may decrease above 5 GHz and constant above 10 GHz. In this paper, P was represented by the upper-bound value observed in Fig. 7.

B. Simulation Results and Discussion

Fig. 8(a) shows the effect of Γ_0 while P_n is the same as P, -60 dB. Because the exact reflection coefficient distribution

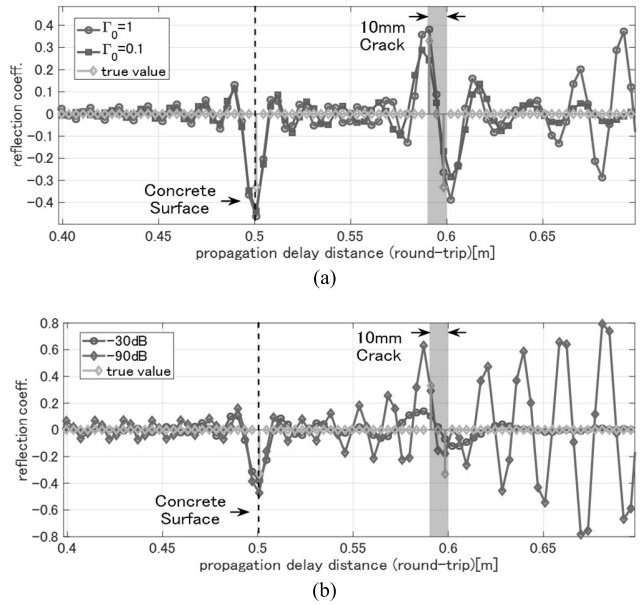

Fig. 8. Reflection coefficient distribution estimated by simulation. (a) Initial reflection coefficient distributions are constant value 1 and 0.1 along distance axis. Both assumed noise level in designing Wiener filter and added noise level are -60 dB. (b) Assumed noise levels in designing Wiener filter are -30 and -90 dB while initial reflection coefficient distribution is constant value 0.1 along distance axis. Added noise level is -60 dB obtained from Fig. 7.

is not known in advance, Γ_0 is assumed to be a certain constant value. In Fig. 8, though the true value of Γ is not constant, Γ is accurately estimated even around the depth of the 10 mm crack without the effect of Γ_0. According to the case $\Gamma_0 = 1$ where the result is overestimated under the crack depth, Γ_0 should be smaller than 1, which is reasonable considering $|\Gamma|$ is 0.6 at most in the case of a crack filled with water in actual data. H_w in (12) and Γ in (11) should be calculated iteratively to obtain more accurate Γ. However, Γ was estimated with enough accuracy without an iteration with Γ_0 above according to Fig. 8(a).

Fig. 8(b) shows the effect of P_n while Γ_0 is 0.1 constant. Because the added noise level is -60 dB, in the case of $P_n = -30$ and -90 dB, SNR is underestimated and overestimated, respectively, causing the underestimation and overestimation of Γ. From Fig. 8(b), P_n should be accurate enough. Nevertheless, in an actual measurement, because P_n depends only on the measurement system, after finding appropriate P_n, P_n can be set constant irrespective of target conditions. In Section V, the noise level is assumed -60-dB white Gaussian noise obtained from Fig. 7 and the initial reflection coefficient distribution is set 0.1 constant.

V. Field Experiment Results and Discussion

To evaluate the effect of the algorithms and operating frequency range on the sensitivity of a system to damages, a field experiment was conducted with a real bridge slab model utilizing an SHF-band measurement system.

A. Measurement System and Modeled Damages

The measurement system consists of double-ridge horn antennas, a network analyzer, data logger, and measurement

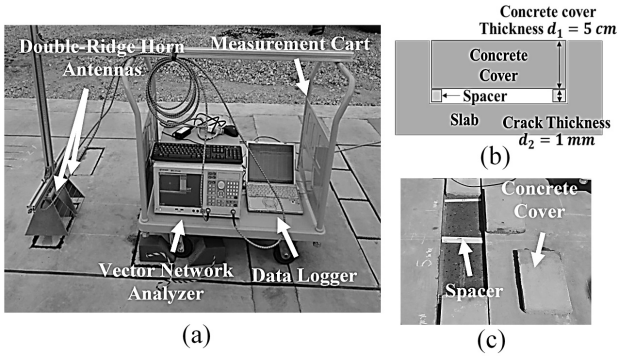

Fig. 9. Measurement system and modeled horizontal crack. (a) Measurement system. (b) Schematic view of horizontal crack. (c) Modeled horizontal crack. Damage thickness is adjusted by inserted spacers' thickness.

cart as shown in Fig. 9(a). Double-ridge horn antenna was used to transmit a wide frequency range including SHF band. Though the system can measure a 2-D radar image, the measurement was conducted at each single point to evaluate the validity of the algorithms. Fig. 9(b) and (c) shows a modeled horizontal crack inside a RC bridge slab. The horizontal crack is modeled by placing a concrete cover on spacers set on a ditch as illustrated in Fig. 9(b). The segregation is modeled by a horizontal crack filled with sand. Damage thickness is adjusted by inserted spacers' thickness.

The results are shown in Section V-B in the case of a 1-mm crack and 2-cm segregation below a concrete surface [Fig. 3(c) and (e)] in dried condition or filled with water, which are typical cases in RC bridge slab monitoring as described in Section I. The results of healthy section is also shown changing the measurement points. The interval of the measurement points is 15 cm in longitudinal direction to evaluate the effect of the rebars whose interval is 20 cm. The transmitted signal is the same as used in the simulation, measured using a steel plate.

B. Field Experiment Results and Discussion

Figs. 10–12 show all the cases including the measured waves and estimated results of a healthy section for the comparison. The theoretical peak values of each layer boundary are also plotted by horizontal dotted lines. The repeatability of all the measured waves of the damages and healthy section is high showing the reasonable reflection coefficient distributions.

Fig. 10(a) shows the measured waves of the segregation with and without water. From Fig. 10(a), though the segregation can be detected by comparing the waves, the depth and condition of the segregation cannot be evaluated. For example, though the largest peaks may be at 0.03 and 0.035 m in the case of segregation without and with water, respectively, because of the large sidelobes, the second peak is not clear, causing the misunderstanding of the two peaks' positions and phase of the reflected waves, which are related to the depth and condition of the damages, respectively.

Fig. 10(b) shows the estimated reflection coefficient distributions of the segregation by time-invariant deconvolution. From Fig. 10(b), a clear negative peak can be found in all the results at the depth of the concrete surface, corresponding to

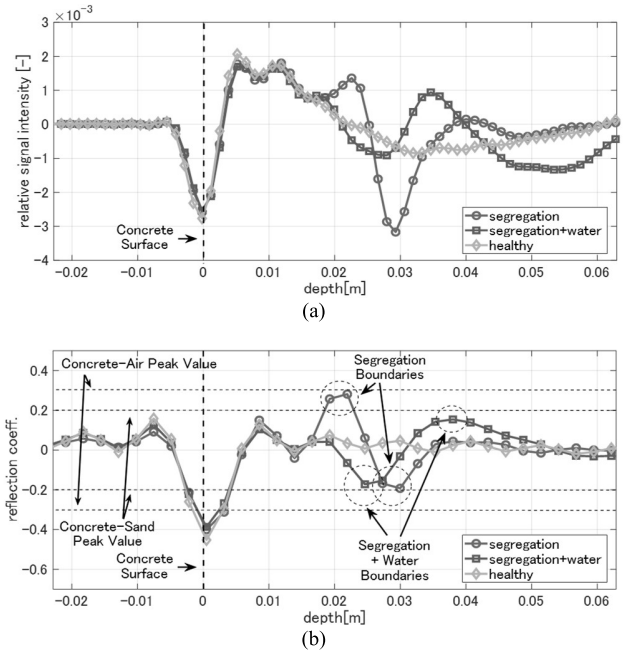

Fig. 10. Measured waves and reflection coefficient distributions of segregation with or without water at field experiment. (a) Measured waves. (b) Time-invariant deconvolution. Depth is calculated considering propagation velocity of electromagnetic wave in concrete medium hereafter.

the reflection coefficient of concrete-air layer boundary, $\Gamma_{ca} = +0.43$. (Therefore, air-concrete layer boundary is -0.3.) At the depth of the damage, the reflection coefficient of the healthy section is almost 0, whereas the dried segregation shows a clear positive–negative peak, corresponding to the reflection coefficient of concrete-sand layer boundary $\Gamma_{cs} = +0.2$ and vice versa. The depth of the peak is reasonable considering the propagation velocity of concrete and segregation medium. On the other hand, the segregation filled with water shows a clear negative–positive peak because the magnitude relation of the permittivity of the two layers is reversed. The reflection coefficient of each boundary is reasonable also in this case, considering the reflection coefficient of concrete-sand-with-water layer boundary $\Gamma_{csw} = -0.2$ and vice versa. From Fig. 10(b), the conclusion is, by time-invariant deconvolution, not only the depth of the segregation but also the existence of water in the segregation can be evaluated from the peak value of the reflection coefficient distribution, which is important in terms of maintenance management.

Fig. 11(a) shows the measured waves of the horizontal crack with and without water. From Fig. 11(a), no clear difference is observed between the waves of the horizontal crack and healthy section because the attenuation of the transmitted signal is significant comparing to the small thickness of the crack. Fig. 11(b) shows the estimated results of the crack by time-invariant deconvolution. From Fig. 11(b), any peaks are not observed below the concrete surface in all the waves. Fig. 11(c) shows the estimated results of the crack by time-variant deconvolution at UHF band. Comparing to the healthy section, only when the crack is filled with water, a large difference is observed. However, because the resolution is decreased utilizing UHF band, the width of the main lobe and

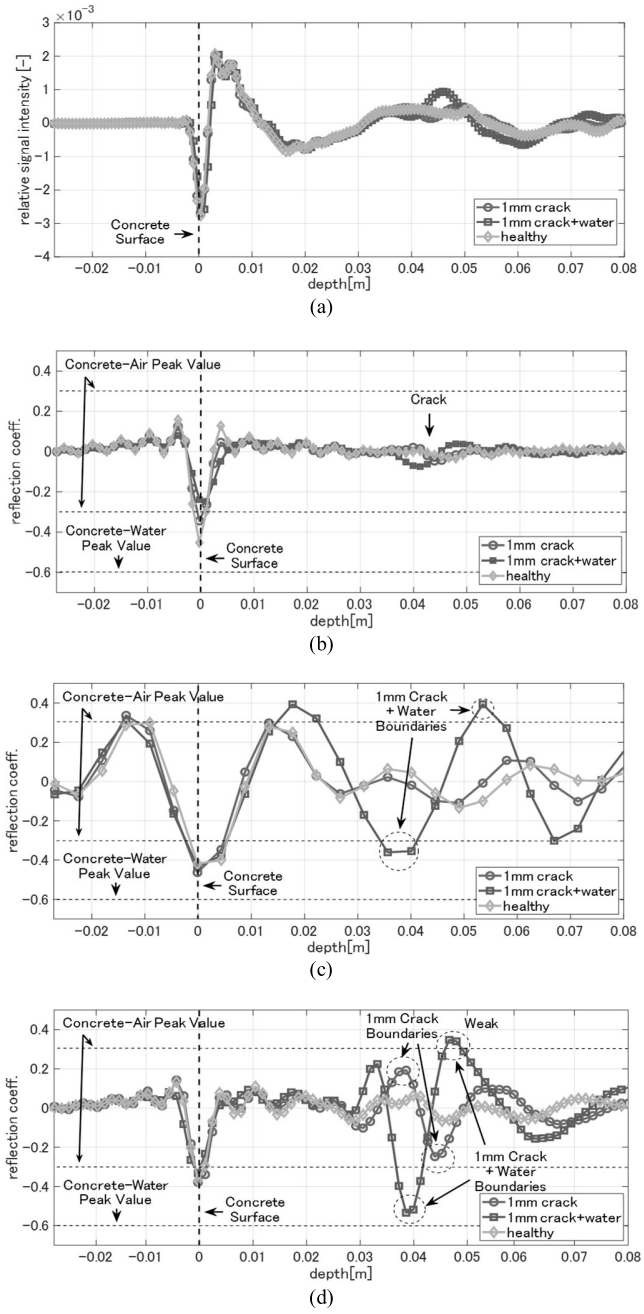

Fig. 11. Measured waves and reflection coefficient distributions of 1-mm crack with or without water at field experiment. (a) Measured waves. (b) Time-invariant deconvolution. (c) Time-variant deconvolution at UHF band. (d) Time-variant deconvolution at SHF band.

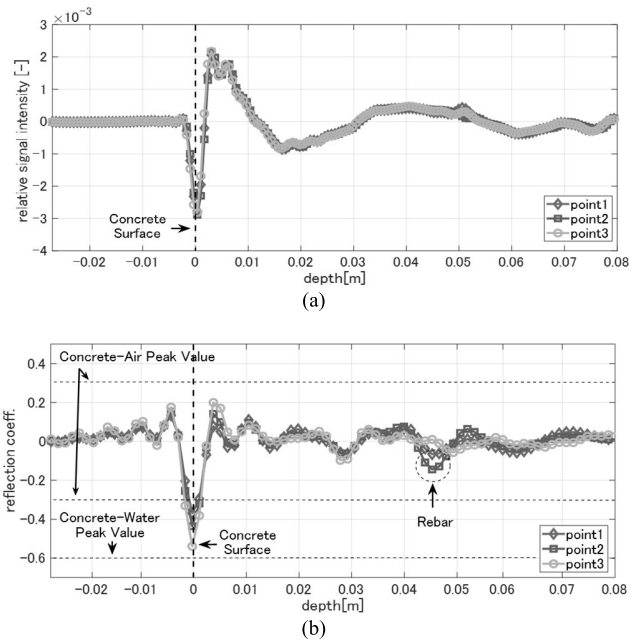

Fig. 12. Measured waves and reflection coefficient distributions of healthy section at field experiment. (a) Measured waves. (b) Time-variant deconvolution at SHF band.

the magnitude of the sidelobe is large, causing the difficulty in specifying the depth of the crack and the existence of water in the crack.

Fig. 11(d) shows the estimated results of the crack by time-variant deconvolution at SHF band. From Fig. 11(d), the reflection coefficient of water-concrete layer boundary is underestimated because the transmission coefficient of concrete-water layer boundary $T_{\mathrm{cw}} = 0.4$ is not considered in the case of the crack filled with water. However, a clear negative peak is observed corresponding to the reflection coefficient of concrete-water layer boundary $\Gamma_{\mathrm{cw}} = -0.6$ at the depth of the boundary. Furthermore, even in the case of the dried crack, a positive–negative peak is found at the appropriate depth. In Fig. 11(d), the errors of the maximum of the peak value to the theoretical value are small, 10% in the case of the crack filled with water and 17% in the case of the dried crack. From Fig. 12, the peak value of the crack is significant comparing to the variation of the healthy section, in which the maximum of the peak is 47% different from Γ_{ca}. For example, the crack is appropriately detected without false detection by setting the threshold of reflection coefficient $\Gamma_{\mathrm{ca}} \pm 30\%$ difference. The peaks in Fig. 12 are considered to be from the rebar, whose amplitudes have variations depending on the distance between the antennas and nearest transverse rebar. From Fig. 11(d), the conclusion is a 1-mm crack is detectable by time-variant deconvolution at SHF band. Then, considering the peak value of the reflection coefficient, even the existence of water in the crack can be detected. The algorithm improves the SNR of the signals by constructing an appropriate filter using the information of the noise and attenuation of the medium.

To summarize Figs. 10–12, damage detection accuracy depends on the types of damages, algorithms, and frequency range. In terms of 2-cm segregation, which is a more severe type of damage than horizontal crack, the depth and existence of water can be evaluated even by time-invariant deconvolution. In terms of 1-mm horizontal crack, however, if the crack is filled with water, which is the easier case considering the reflection coefficient of concrete-water layer boundary, the crack can be detected by time-variant deconvolution. If the crack is dried, which is considered to be the most difficult case, the crack can be detected only by the combination of time-variant deconvolution and SHF band. The peak value of the reflection coefficient distribution of each damage is significant comparing to the variation of the healthy section.

VI. Conclusion

In this paper, we proposed a new damage detection algorithm based on deconvolution. First, based on the defined inverse problem, we proposed two types of algorithms, time-invariant deconvolution and time-variant deconvolution. The difference is whether the effect of attenuation is considered or not, though in time-variant deconvolution a noise reduction filter is necessary because of its characteristics of amplifying noise. Then, to apply the proposed algorithms, because the electromagnetic properties of concrete at SHF band is not clear in terms of bridge slab concrete constructed by the Japanese standard configuration, the measurements were conducted to estimate the permittivity and attenuation coefficient of the concrete. The proposed noise reduction filter was validated in simulation, in which the reflection coefficient was accurately estimated when SNR was appropriately assumed irrespective of initial reflection coefficient distribution. Finally, the damage detection accuracy of each algorithm is discussed with field experiment data. The conclusion is, in terms of segregation, though it is detectable by comparing the measured waves, the depth and condition of the segregation can be evaluated by time-invariant deconvolution. In terms of horizontal crack, however, a 1-mm horizontal crack is not detected by measured waves or time-invariant deconvolution because the attenuation of the transmitted signal is significant. Though the 1-mm crack filled with water is detectable by time-variant deconvolution at UHF band, the 1-mm dried crack is not detected because of the target crack condition and resolution of the system. The 1-mm dried crack is detected only by time-variant deconvolution at SHF band, in which the algorithm restores the resolution of the system by greatly emphasizing the peaks of the reflection coefficient distributions of the target crack.

The obtained concrete properties are expected to be applicable to the most of common RC bridge slabs following the Japanese standard as indicated in Section III. However, in the case of the concrete structures of different standards, because the electromagnetic properties of concrete are different because of the difference of concrete composition, this may not be true. At least, the same algorithms are applicable to the countries of the references without any additional experiments [30], [31]. By experimentally accumulating the knowledge of the relationship between concrete composition and electromagnetic properties of concrete utilizing the methodology proposed in this paper, the algorithms are also applicable to the concrete structures in different countries.

Appendix A

This appendix explains the derivation of the Wiener filter H_w and the revised transmitted signal E_t' defined by (12) and (13). To simplify the problem, considering the received wave E_{obs} generated from Γ_z at z, the Fourier transform of (11) is equal to

$$E_{\text{obs}}(f) = \Gamma_z \times E_t(f) + n(f) \tag{24}$$

at each f. If the reflected signal $\Gamma_z \times E_t$ is small comparing to the noise n, E_{obs} is represented by

$$E_{\text{obs}}(f) \approx n(f) \tag{25}$$

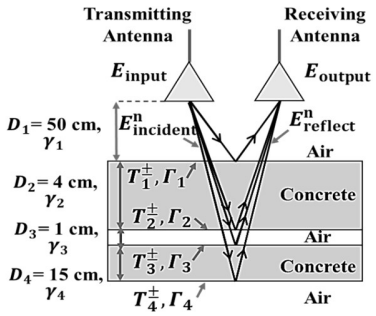

Fig. 13. Simulation conditions and received signal derivation of 1-D bridge slab model.

where E_{obs} is dominated by n. The solution of (24) for Γ_z, Γ_z^{est} derived by (2) is equal to

$$\Gamma_z^{\text{est}} \approx n(f)/E_t(f) \tag{26}$$

where Γ_z^{est} is meaningless when the reflected signal $\Gamma_z \times E_t$ is smaller than n because Γ_z^{est} is dominated by n. Also because of the attenuation of E_t, Γ_z^{est} estimated by (26) shows unstable behavior at deeper depth affected by amplified n. A signal processing is needed which prevents Γ_z^{est} from diverging when the power of $\Gamma_z \times E_t$ is close to or falls below that of n.

The Wiener filter H_w is a frequency domain time-invariant filter to obtain a noise-free signal $\Gamma_z \times E_t$ from a noise-contaminated signal E_{obs} in (24)

$$\Gamma_z \times E_t(f) \approx H_w(f) \times E_{\text{obs}}(f) \tag{27}$$

where H_w is the function of the power spectrum P of each signal [26]. Dividing both sides of (27) by H_w and defining the revised transmitted signal E_t' as (13), (27) and (2) are rewritten as

$$E_{\text{obs}}(f) \approx \Gamma_z \times E_t'(f) \tag{28}$$

$$\Gamma_z(f) \approx E_{\text{obs}}(f)/E_t'(f) \tag{29}$$

using E_t', respectively. If P_n is large, H_w becomes small from (12), and E_t' becomes large from (13), making Γ_z small from (29). The noise effect is appropriately suppressed in (29).

One problem is that the distribution of $\Gamma(z)$ cannot be obtained from (29) because H_w is determined for only one $\Gamma = \Gamma_z$. Nevertheless, assuming the order of $P_{\Gamma \times E_t}$ is approximately determined by Γ at $z = ct$ and E_t at t, using H_w at each t, (29) is extended to any z and solved by the same procedure for deriving (6). The assumption is valid considering the estimation results in Sections IV and V, possibly because the number of layer boundary is limited so that the effect of the distribution of $\Gamma(z)$ is not so large to determine the order of $P_{\Gamma \times E_t}$.

Appendix B

This appendix explains the simulation method used in Section IV, the same as proposed in [32] and [34]. In simulation, noise is added to an received signal to validate the effect of the filter. The received signal itself is derived from an analytical solution of 1-D bridge slab model as shown in Fig. 13. The incident signal at each medium boundary

E^n_{incident} is provided by

$$E^n_{\text{incident}} = \prod_{i=1}^{n-1} \left(T_i^+ T_i^-\right) \prod_{i=1}^{n} (e^{-2D_i\gamma_i}) E_{\text{input}} \tag{30}$$

where E_{input} is the input signal transmitted from an antenna, D_i and γ_i are the thickness and propagation constant of each medium, which includes the attenuation effect, and $T_i^{\pm}$ is the two-way transmission coefficient (medium i to $i+1$ and medium $i+1$ to i) between the media. The reflected signal E^n_{reflect} at each boundary and the received signal E_{output} is provided by

$$E^n_{\text{reflect}} = \Gamma_n E^n_{\text{incident}} \tag{31}$$

$$E_{\text{output}} = \sum_n E^n_{\text{reflect}} \tag{32}$$

where Γ_n is the reflection coefficient at each medium boundary. Γ_n inversely estimated from E_{output} is expected to be exactly the same as the assumed reflection coefficient in the case of no noise condition.

In the simulation results shown in Fig. 8, the assumed thickness of the media is 50-cm air layer, 4-cm concrete layer, 1-cm air layer, and 15-cm concrete layer. Below the 15-cm concrete layer is filled with air layer, which is intended to simulate real bridge slab measurement configurations. All the electromagnetic properties of each medium are following the discussions in Section III.

ACKNOWLEDGMENT

The authors would like to thank Prof. K. Maekawa from the Department of Urban Innovation, Yokohama National University, Yokohama, Japan, Prof. I. Iwaki from the Department of Civil Engineering, Nihon University, Tokyo, Japan, Prof. A. Hirose from the Department of Electrical Engineering and Information Systems, The University of Tokyo, Tokyo, and Dr. W. Tsujita from the Advanced Technology Research and Development Center, Mitsubishi Electric Corporation, Tokyo, for the helpful comments and supports for the research.

REFERENCES

[1] J. Hugenschmidt, "Concrete bridge inspection with a mobile GPR system," *Construct. Building Mater.*, vol. 16, no. 3, pp. 147–154, Apr. 2002.

[2] A. M. Alani, M. Aboutalebi, and G. Kilic, "Applications of Ground Penetrating Radar (GPR) in bridge deck monitoring and assessment," *J. Appl. Geophys.*, vol. 97, pp. 45–54, Oct. 2013.

[3] A. Loizos and C. Plati, "Accuracy of pavement thicknesses estimation using different ground penetrating radar analysis approaches," *NDT&E Int.*, vol. 40, no. 2, pp. 147–157, Mar. 2007.

[4] A. Benedetto, F. Benedetto, M. R. De Blasiis, and G. Giunta, "Reliability of radar inspection for detection of pavement damage," *Road Mater. Pavement Des.*, vol. 5, no. 1, pp. 93–110, 2004.

[5] A. Benedetto, G. Manacorda, A. Simi, and F. Tosti, "Novel perspectives in bridges inspection using GPR," *Nondestruct. Test. Eval.*, vol. 27, no. 3, pp. 239–251, Aug. 2012.

[6] I. L. Al-Qadi and S. Lahouar, "Use of GPR for thickness measurement and quality control of flexible pavements," *J. Assoc. Asphalt Paving Technol.*, vol. 73, pp. 501–528, Jan. 2004.

[7] A. Benedetto, F. Tosti, L. B. Ciampoli, and F. D'Amico, "An overview of ground-penetrating radar signal processing techniques for road inspections," *Signal Process.*, vol. 132, pp. 201–209, Mar. 2016.

[8] T. Saarenketo and T. Scullion, "Road evaluation with ground penetrating radar," *J. Appl. Geophys.*, vol. 43, pp. 119–138, Mar. 2000.

[9] S. Zhao and I. L. Al-Qadi, "Development of an analytic approach utilizing the extended common midpoint method to estimate asphalt pavement thickness with 3-D ground-penetrating radar," *NDT&E Int.*, vol. 78, pp. 29–36, Nov. 2015.

[10] S. Zhao and I. L. Al-Qadi, "Development of regularization methods on simulated ground-penetrating radar signals to predict thin asphalt overlay thickness," *Signal Process.*, vol. 132, pp. 261–271, Mar. 2017.

[11] F. Benedetto and F. Tosti, "A signal processing methodology for assessing the performance of ASTM standard test methods for GPR systems," *Signal Process.*, vol. 132, pp. 327–337, Mar. 2017.

[12] D. J. Daniels, *Ground Penetrating Radar*, 2nd ed. London, U.K.: IET, 2004, pp. 73–129.

[13] H. M. Jol, *Ground Penetrating Radar Theory and Applications*, 1st ed. Oxford, U.K.: Elsevier, 2009, pp. 41–72.

[14] Ministry of Land, Infrastructure, Transport and Tourism. *Road Maintenance in Japan: Problems and Solutions*. Accessed: Jul. 17, 2018. [Online]. Available: http://www.mlit.go.jp/road/road_e/pdf/RoadMaintenance.pdf

[15] National Institute for Land and Infrastructure Management. *Research on Durability Assessment of Concrete Slab of Existing Road Bridge*. (in Japanese). Accessed: Jul. 17, 2018. [Online]. Available: http://www.mlit.go.jp/chosahoko-ku/h25giken/program/kadai/pdf/ippan/anzen1_07.pdf

[16] T. Mizutani, N. Nakamura, T. Yamaguchi, M. Tarumi, Y. Ando, and I. Hara, "Bridge slab damage detection by signal processing of UHF-band ground penetrating radar data," *J. Disaster Res.*, vol. 12, no. 3, pp. 415–421, Aug. 2017.

[17] S. M. Riad, "The deconvolution problem: An overview," *Proc. IEEE*, vol. 74, no. 1, pp. 82–85, Jan. 1986.

[18] O. Yilmaz, *Seismic Data Analysis: Processing, Inversion, and Interpretation of Seismic Data*, 2nd ed. Tulsa, OK, USA: Society of Exploration Geophysicists, 2001, pp. 159–270.

[19] K. L. Peacock and S. Treitel, "Predictive deconvolution: Theory and practice," *Geophysics*, vol. 34, no. 2, pp. 155–169, Oct. 1969.

[20] C. Schmelzbach, F. Scherbaum, J. Tronicke, and P. Dietrich, "Bayesian frequency-domain blind deconvolution of ground-penetrating radar data," *J. Appl. Geophys.*, vol. 75, no. 4, pp. 615–630, Dec. 2011.

[21] S. H. Bickel and R. R. Natarajan, "Plane-wave Q deconvolution," *Geophysics*, vol. 5, no. 9, pp. 1426–1439, Sep. 1985.

[22] J. D. Irving and R. Knight, "Removal of wavelet dispersion from ground-penetrating radar data," *Geophysics*, vol. 68, no. 3, pp. 960–970, May 2003.

[23] X. Zhang, *Linear Algebra for Signal Processing*, (in Japanese), 1st ed. Tokyo, Japan: Morikita, 2008, pp. 149–201.

[24] F. Roth, *Convolutional Models for Landmine Identification With Ground Penetrating Radar*, 1st ed. Delft, The Netherlands: Delft Univ. Press, 2004, pp. 13–62.

[25] R. Persico, *Introduction to Ground Penetrating Radar*, 1st ed. Hoboken, NJ, USA: Wiley, 2014, pp. 48–77.

[26] L. L. Scharf, *Statistical Signal Processing*, 1st ed. Boston, MA, USA: Addison-Wiley, 1991, pp. 312–313.

[27] I. L. Al-Qadi, O. A. Hazim, W. Su, and S. M. Riad, "Dielectric properties of Portland cement concrete at low radio frequencies," *ASCE J. Mater. Civil Eng.*, vol. 7, no. 3, pp. 192–198, Aug. 1995.

[28] H. W. Whittington, J. McCarter, and M. C. Forde, "The conduction of electricity through concrete," *Mag. Concrete Res.*, vol. 33, no. 114, pp. 48–60, Mar. 1981.

[29] A. Robert, "Dielectric permittivity of concrete between 50 MHz and 1 GHz and GPR measurements for building materials evaluation," *J. Appl. Geophys.*, vol. 40, nos. 1–3, pp. 89–94, Oct. 1998.

[30] C. Patriarca, S. Lambot, M. R. Mahmoudzadeh, J. Minet, and E. Slob, "Reconstruction of sub-wavelength fractures and physical properties of masonry media using full-waveform inversion of proximal penetrating radar," *J. Appl. Geophys.*, vol. 74, pp. 26–37, May 2011.

[31] C.-H. Chen, C.-L. Liu, C.-C. Chiu, and T.-M. Hu, "Ultra-wide band channel calculation by SBR/image techniques for indoor communication," *J. Electromagn. Waves Appl.*, vol. 20, no. 1, pp. 41–51, Sep. 2006.

[32] J. L. Volakis, R. C. Johnson, and H. Jasik, *Antenna Engineering Handbook*, 4th ed. New York, NY, USA: McGraw-Hill, 2007, pp. 55-1–55-23.

[33] Keysight Technologies. *Basics of Measuring the Dielectric Properties of Materials*. Accessed: Jul. 17, 2018. [Online]. Available: http://literature.cdn.keysight.com/-litweb/pdf/5989-2589EN.pdf?id=670519&cc=NL&lc=dut

[34] W. H. Hayt, *Engineering Electromagnetics*, 8th ed. New York, NY, USA: McGraw-Hill, 2012, pp. 406–452.

Takahiro Yamaguchi was born in Tokyo, Japan, in 1991. He received the B.S. and M.S. degrees in civil engineering from The University of Tokyo, Tokyo, Japan, in 2015 and 2017, respectively, where he is currently pursuing the Ph.D. degree with the Department of Civil Engineering, Graduate School of Engineering.

His research interests included signal processing and deep learning of ground penetrating radar images, and monitoring of bicycle lane by dynamic response of the bicycle. His research interests include structural health monitoring of infrastructure, especially bridge slab and road pavement.

Tsukasa Mizutani (M'18) was born in Osaka, Japan, in 1983. He received the B.S. degree in urban engineering, and the M.S. and Ph.D. degrees in civil engineering from The University of Tokyo, Tokyo, Japan, in 2007, 2009, and 2011, respectively.

He was an Assistant Professor with the Department of Civil Engineering, School of Engineering, The University of Tokyo, from 2011 to 2017. He has been a Project Lecturer with the Institute of Industrial Science, The University of Tokyo since 2017. His research interests include digital signal processing and electromagnetic wave measurement for structural health monitoring.

Dr. Mizutani was a recipient of the Paper Award for Young Scientists from the Japan Society of Hydrology and Water Resources in 2015 and the Best Paper Award from the Japan Association for Wind Engineering in 2017.

Minoru Tarumi was born in Osaka, Japan, in 1955.

He joined the C. E. Management Integrated Laboratory Co., Ltd., Osaka, in 2014, where he is currently the General Manager. He is involved in the radar measurement and analysis professional, and has conducted many radar investigations for several decades.

Mr. Tarumi is a member of the Japan Society of Civil Engineers and the Society of Exploration Geophysicists of Japan.

Di Su received the B.S. and M.S. degrees in civil engineering from Tsinghua University, Beijing, China, and the Ph.D. degree in civil engineering from The University of Tokyo, Tokyo, Japan.

He gained experience in full-scale testing and structural modeling, and also examined strategies for vibration monitoring. He is currently an Assistant Professor with The University of Tokyo. His research interests include structural engineering, bridge maintenance, and remote sensing using microwave radar and vision technology.